Crystalline Bis-urea Nanochannel Architectures Tailored for Single-File Diffusion Studies

Clifford R. Bowers,*,†,⊥ Muslim Dvoyashkin,†,§ Sahan R. Salpage,‡ Christopher Akel,† Hrishi Bhase,† Michael F. Geer,‡ and Linda S. Shimizu*,‡,⊥

†Department of Chemistry, University of Florida, Gainesville, Florida 32611, United States and ‡Department of Chemistry and Biochemistry, University of South Carolina, Columbia, South Carolina 29208, United States. ⊥C.R.B and L.S.S. contributed equally to this work. §Present address: Institute of Chemical Technology, Universität Leipzig, 04103 Leipzig, Germany.

ABSTRACT Urea is a versatile building block that can be modified to self-assemble into a multitude of structures. One-dimensional nanochannels with zigzag architecture and cross-sectional dimensions of only ~3.7 Å × 4.8 Å are formed by the columnar assembly of phenyl ether bis-urea macrocycles. Nanochannels formed by phenylethynylene bis-urea macrocycles have a round cross-section with a diameter of ~9.0 Å. This work compares the Xe atom packing and diffusion inside the crystalline channels of these two bis-ureas using hyperpolarized Xe-129 NMR. The elliptical channel structure of the phenyl ether bis-urea macrocycle produces a Xe-129 powder pattern line shape characteristic of an asymmetric chemical shift tensor with shifts extending to well over 300 ppm with respect to the bulk gas, reflecting extreme confinement of the Xe atom. The wider channels formed by phenylethynylene bis-urea, in contrast, present an isotropic dynamically average electronic environment. Completely different diffusion dynamics are revealed in the two bis-ureas using hyperpolarized spin-tracer exchange NMR. Thus, a simple replacement of phenyl ether with phenylethynylene as the rigid linker unit results in a transition from single-file to Fickian diffusion dynamics. Self-assembled bis-urea macrocycles are found to be highly suitable materials for fundamental molecular transport studies on micrometer length scales.

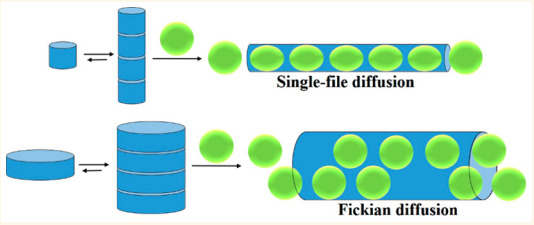

KEYWORDS: xenon-129 · nanotubes · bis-urea · single-file diffusion · hyperpolarization · SEOP · spin-exchange optical pumping

Urea is a versatile molecular building block that can be modified to self-assemble into a multitude of structures, including pillars, fibers, sheets, tapes, capsules, and gels.[1−4] The urea NH groups serve as hydrogen bond donors, while the urea oxygen is an excellent acceptor. The bis-urea macrocycles (Figure 1) consist of two urea groups and two rigid C-shaped spacers that allow the macrocycle to adopt a relatively planar conformation with the urea groups oriented approximately perpendicular to the plane of the macrocycle, a conformation favoring high fidelity columnar assembly.[5−12] Phenylether bis-urea (**1**) and phenylethynylene bis-urea (**2**) self-assemble into similar columnar structures held together by hydrogen bonds with distances of 2.85−3.05 Å, which set a repeat distance of between 4.6 and 4.7 Å.[6,10] The cross-sectional size and shape of the columns differ as they are precisely determined by the molecular structure of the macrocycle building blocks. In **1**, the cavity is seen to be roughly elliptical in shape with cross-sectional dimensions of ~4.8 Å × 3.7 Å, while in **2**, the pore space cross-section is almost round with a diameter of ~9 Å. The columns pack together to give molecular crystals with aligned channels. Figure 2 compares the X-ray structures of **1** and **2** through views down the *b* axis of seven neighboring columns to show the spatial arrangement and homogeneity of these simple columns. Heating removes the crystallization solvent.

The pore spaces of the bis-urea materials assembled from **1** and **2** have not been previously explored by Xe NMR. As can be seen in the space-filling model shown in Figure 1, two Xe atoms (collision diameter of 4.4 Å) are unable to fit side-by-side within the cavity of **1**, and hence, Xe atoms adsorbed into the one-dimensional channels formed by stacking of **1** are expected to exhibit single-file molecular packing and

* Address correspondence to bowers@chem.ufl.edu, shimizls@mailbox.sc.edu.

Received for review March 29, 2015 and accepted June 2, 2015.

Published online June 02, 2015
10.1021/acsnano.5b01895

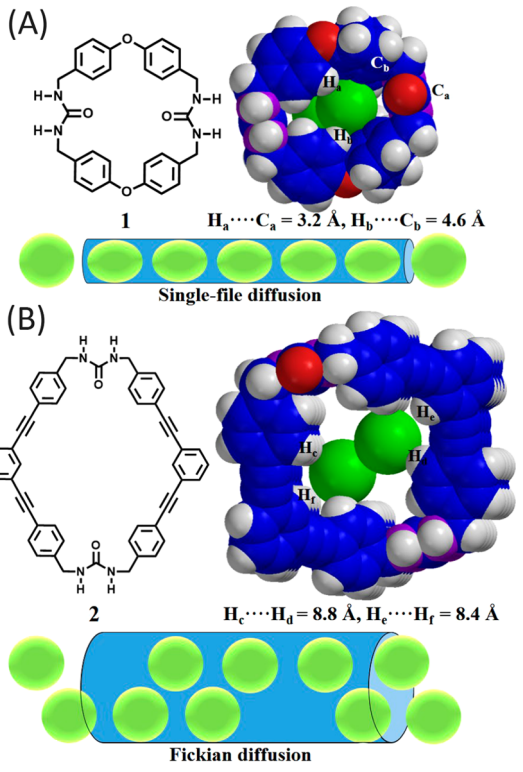

Figure 1. Xe atom diffusion studied in channels of two different self-assembled bis-urea macrocycles. (A) Phenyl ether bis-urea 1 displays an internal diameter of 0.48 nm × 0.37 nm.[6,10] Xe has a collision diameter of 0.44 nm and is depicted in the tube for comparison. (B) The phenylethynylene bis-urea macrocycle 2 forms nanotubular structures with internal diameters of approximately 0.9 nm,[10] significantly larger than the Xe atom. Thus, it is possible for two Xe atoms to pass within macrocycle 2, but not in macrocycle 1.

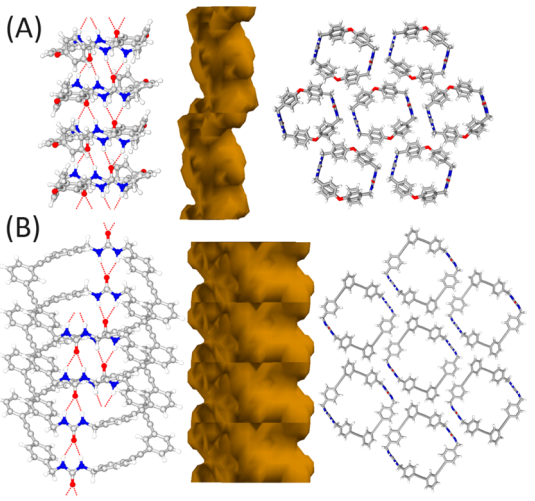

Figure 2. Comparison of the X-ray structures of two different bis-urea macrocycles. (A) Self-assembly of phenyl ether bis-urea macrocycle 1 affords columns *via* hydrogen bonding and edge-to-face aryl-stacking interactions.[6] Mercury was used to calculate the interior channel surface (in brown) from the CIF file of host 1 · AcOH after removal of the solvent.[64] The packing of the columns in the crystal structure is illustrated by the view along the *b*-axis of seven hydrogen-bonded tubes (AcOH guests omitted). (B) Self-assembly of phenylethynylene bis-urea macrocycle 2 affords similar columns that are held together through the urea hydrogen-bonding motif.[10] A representation of the interior channel surface (in brown) was calculated from host 2 · nitrobenzene after removal of the solvent.[64] A similar view along the *b*-axis of seven hydrogen-bonded tubes (nitrobenzene guests omitted) shows the arrangement and larger relative diameter of the channels of 2 in comparison to 1.

transport characteristics. Macrocycle **2**, on the other hand, has a larger cavity with a diameter of ~9 Å, just wide enough to accommodate two Xe atoms. Here, we employ hyperpolarized (HP) ^{129}Xe to examine the effects of these structural differences on Xe packing and unidimensional diffusion dynamics within the channels formed by self-assembly of **1** and **2**. We introduce the concept of transitioning between normal Fickian diffusion (ND) to single-file diffusion based on rational design of supramolecular channel architectures utilizing the bis-urea assembly motif.

Single-file diffusion (SFD) is a collective many-body phenomenon occurring in systems of random walkers confined to one-dimensional channels under certain conditions. In its simplest embodiment, SFD is a manifestation of correlated random displacements in a one-dimensional lattice gas subject to interparticle exclusion interaction. Like pearls on a string, the sequential order of particles in the file is time-invariant,[13] and the random-walk (RW) displacements are suppressed. SFD has been studied intensively in various macroscopic channel-particle constructs with the aim of validating single-file transport models and theoretical simulations.[14−19]

Single-file transport on the molecular scale has important potential applications. The recent demonstration of single-file transport for controlled release of protein drugs through cylindrical nanochannels formed in a microfabricated block copolymer membrane provides an elegant example of the power of this approach.[20] In principal, single-file nanochannels can also be exploited for energetically efficient separations, for instance, in a mixture of small (S) and large (L) gas molecules which independently exhibit ND and SFD, respectively. If S may pass S or L, S retains its high mobility with ND time-scaling, allowing it to be efficiently separated from L. This property could also be beneficial in catalysis where L is converted to S, since a low single-file mobility of L is favorable for a long contact time with active sites while the product S molecules rapidly diffuse away from the active sites. However, realization of such applications requires SFD to be well-understood first in single-component single-file conditions. Fundamental studies require channel persistence lengths sufficient to allow the SFD regime to be obtained within the experimental detection time-window.[21−27,28,29,30−32] Furthermore, channels must be free of obstructions and defects where molecules might pass one another.

The exploration of crystalline materials composed of one-dimensional channel structures with sub-nanometer cross-sectional dimensions has proven to be one of the most intriguing uses of ^{129}Xe NMR.[24−26,31−42] The ^{129}Xe peak for the adsorbed phase

of Xe in sub-nanometer diameter channels is typically well-resolved from the bulk gas peak, and the ^{129}Xe chemical shift depends on channel architecture, cross-sectional dimensions, chemical composition, loading, dynamics, and channel orientation in the static magnetic field. Distortions from spherical symmetry resulting from intermolecular interactions induce a paramagnetic deshielding of the ^{129}Xe nucleus relative to the free atom. Hence, the chemical shift anisotropy inside one-dimensional channels depends on both Xe-channel and Xe−Xe interactions.[43,44] In channels too narrow for Xe atoms to pass one another, single-file packing and diffusion effects can be seen by ^{129}Xe NMR with a clarity and detail unparalleled by any other technique. These effects have been reported in various types of porous solids with one-dimensional channels, including TPP,[24,37] dipeptides (L-alanyl-L-valine, L-valyl-L-alanine),[25,31,32,38,41] molecular sieves[44] (*e.g.*, ALPO-11,[33,36] ALPO-5,[34] SSZ-24[45]), and transition-metal molecular wheels.[26] In diamagnetic porous media, where the ^{129}Xe spin−lattice relaxation time can be exceedingly long (ca. 200 s in AV at low loading),[24,25] conventional thermally polarized NMR experiments can be impractical. In such cases, NMR studies can be facilitated by ^{129}Xe hyperpolarization (HP) signal enhancement afforded by Rb−Xe spin-exchange optical pumping (SEOP).[45−53]

A most decisive observation of small molecule single-file diffusion was achieved in the crystalline L-alanine-L-valine (AV) nanotubes, where a combination of high-gradient PFG-NMR measurements at 17.6 T and HP ^{129}Xe spin tracer exchange (HSTE) NMR revealed Xe in AV to be a highly ideal single-file system.[31] HSTE-NMR is a variant of conventional tracer exchange[54−61] based on the selective saturation−recovery pulse sequence with the nuclear spin serving as the sorbate tracer label.[25] Signal enhancements obtained with ^{129}Xe SEOP enable diffusion dynamics to be probed in an observation time window spanning more than 3 orders of magnitude (ca. 10 ms -200 s). The ^{129}Xe HSTE data obtained in AV was found to be in essentially perfect compliance with a fully determined SFD model with no fitting parameters.[31,32] Whether or not nanotubular bis-ureas can serve as similarly ideal hosts, but with the advantage of variability in channel architecture, is one of several questions that is addressed in the present study.

Taking advantage of the ~10^4-fold NMR signal enhancement afforded by ^{129}Xe SEOP, we explore the intermolecular Xe−wall and Xe−Xe interactions within the nanotubular structures formed by **1** and **2** as a function of the Xe overpressure. In **1**, distortion from spherical symmetry leads to a strong anisotropy of the chemical shift tensor indicative of extreme confinement and single-file Xe adsorption. We examine the effect of enlarging the center cavity of the bis-urea macrocycle on the ^{129}Xe line shape and its loading dependence. Additionally, we utilize ^{129}Xe HSTE NMR to characterize Xe diffusion dynamics within the nanochannels of **1** and **2**. We investigate the effects of a simple replacement of phenyl ether with phenylethynylene as the rigid linker unit on the unidimensional diffusion dynamics.

RESULTS AND DISCUSSION

Hyperpolarized Xenon-129 NMR Spectroscopy. The isolated Xe atom has a purely diamagnetic shielding. Distortions from spherical symmetry resulting from intermolecular interactions induce paramagnetic excitations which deshield the ^{129}Xe nucleus relative to the free atom. Hence, the chemical shift anisotropy inside one-dimensional channels depends on Xe−channel and Xe−Xe interactions.[38,43,44] The cross-section of **1** may be superficially described as elliptical, with dimensions 3.7 Å × 4.8 Å for the interior van der Waals surface estimated from the crystal structure.[62] The minor axis of the elliptical center cavity of **1** is substantially smaller than the collision diameter of the Xe atom of 4.4 Å. Hence, passage of a Xe atom through the macrocycle **1** requires a correspondingly large distortion of its electron density. Clearly, two Xe atoms are unable to fit side-by-side in the channels formed by stacking of **1**. In the larger channels formed by stacking of **2**, Xe is not so tightly confined, and a more isotropic dynamically averaged electronic environment is predicted. Figure 2 shows representations of the interior channels (in brown) calculated using Mercury[63] from the reported crystal structures of the hosts with the solvent of crystallization removed.[64] Due to the geometry of the stabilizing aryl stacking and alkyne to phenyl interactions, the walls of the channels formed by **1** or **2** are not smooth on the atomic scale. Thus, Xe−wall interactions (and hence the transverse components of the shielding tensor) will vary periodically along the channel axis but are dynamically averaged when Xe diffusion is sufficiently fast.

The theory paper of Jameson *et al.*[44] provides valuable guidance on how to interpret the ^{129}Xe lineshapes observed in the bis-urea **1** crystals. Lineshapes in the smooth, round "narrow-bore pipe" channel, where the minimum potential energy occurs with the Xe atom at the center of the pipe, reflect the axially symmetric shielding tensor with principal values $\sigma_{xx} = \sigma_{yy} = \sigma_{\perp}$, where the *z*-principal axis is taken to be parallel to the channel axis. The electron density of the isolated Xe atom is football shaped. Due to the paramagnetic excitation, the Xe nucleus is most strongly deshielded along the channel axis (*i.e.*, $\sigma_{\parallel} < \sigma_{\perp}$). With increased loading, Xe−Xe interactions compress the electron density along the channel axis, thereby increasing $\sigma_{\perp}$ while $\sigma_{\parallel}$ remains unaffected.[44] Anisotropy decreases as loading increases. When the Xe−wall and Xe−Xe interactions are balanced, $\sigma_{\parallel} - \sigma_{\perp} \rightarrow 0$ and a symmetric isotropic NMR line shape is observed. At still higher

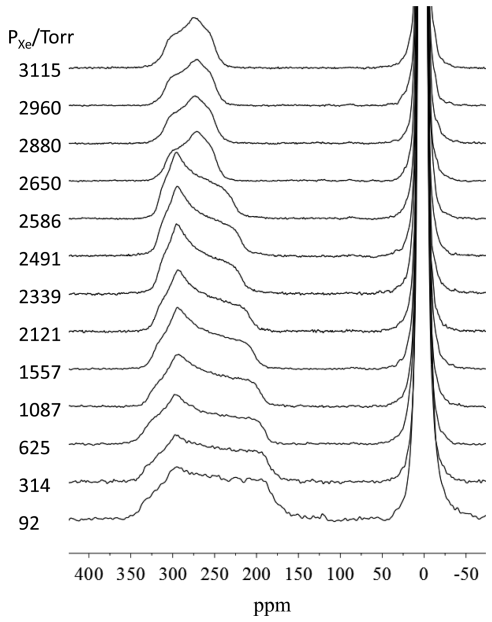

Figure 3. Dependence of the HP ^{129}Xe NMR spectrum of phenyl ether bis-urea macrocycle 1. Experiments were conducted using He/Xe mixture with a total pressure of 3115 Torr (25 °C).

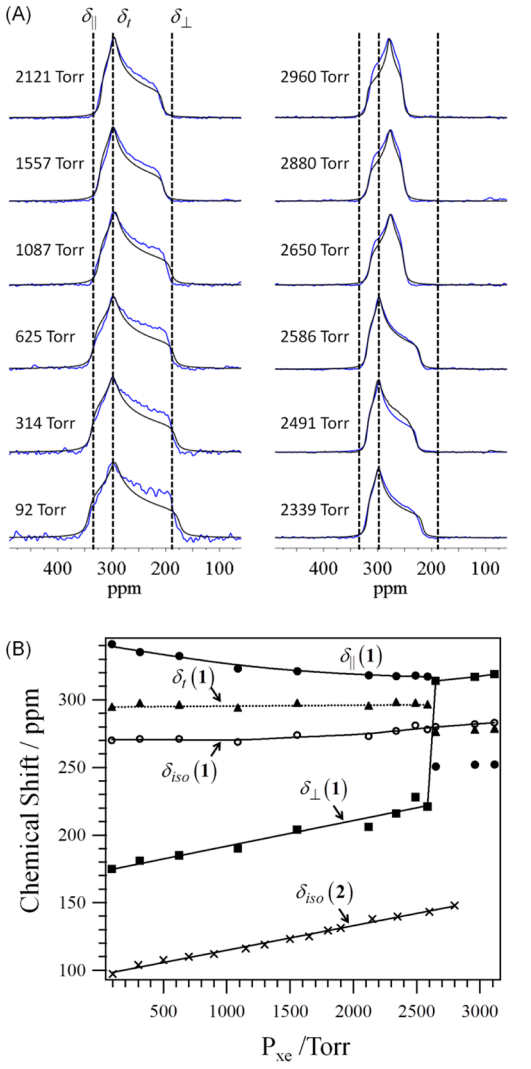

Figure 4. (A) Chemical shift powder pattern fits to the HP ^{129}Xe lineshapes in the channels of macrocycle 1 as a function of the Xe partial overpressure. (B) Summary plot of best fitted values for the principal values of the ^{129}Xe chemical shift tensor for macrocycle 1 ($\delta_{\parallel}$, filled circles; δ_t, triangles; $\delta_{\perp}$, squares; $\delta_{iso}(1)$, open circles; isotropic shifts in macrocycle 2 ($\delta_{iso}(2)$, crosses). Linear least-squares fits gave $\delta_{\perp} = (0.019 \pm 0.002)P_{Xe} + 173 \pm 3$ and $\delta_{iso}(2) = (0.0182 \pm 0.0004)P_{Xe} + 96.7 \pm 0.7$. The slope of δ_t is essentially zero up to the discontinuity.

loading, the anisotropy may reverse sign, as in AV,[25,38] VA,[38] and TPP.[24,37]

Figure 4 in the work of Jameson[44] illustrates the effect of elongation into an elliptical cross-section, where reduced symmetry yields three unique principal shielding tensor components, $\sigma_{\parallel} \neq \sigma_t \neq \sigma_{\perp}$, where σ_t is the shielding component along the minor axis. The observed shielding tensor depends on the orientation of approach of two Xe atoms in the channel and is thus highly sensitive to the channel architecture. In the roughly elliptical channels of the zeolite ALPO-11,[36,44] the experimental loading dependence of the ^{129}Xe powder pattern was analyzed in detail using a dynamic averaging model based on a statistical distribution of Xe site types consisting of zero, one, or two adjacent Xe atoms, where elliptical pores are interconnected in a zigzag arrangement.[36] The narrower channels of the bis-urea **1** crystals may also be described as zigzag shaped (see Figure 2A).

Figure 3 presents the HP ^{129}Xe spectra of **1** recorded at a series of Xe pressures between ~100 and ~3000 Torr at 25 °C. Despite severe steric hindrance, we are nevertheless able to detect the NMR signal of HP ^{129}Xe adsorbed inside the channels formed by **1**. As expected for such extreme confinement, a broad powder pattern is observed with chemical shifts extending to >300 ppm at low loading. The fits to a single idealized chemical shift tensor powder pattern line shape are superimposed on the experimental spectra in Figure 4A. The agreement is not perfect but is considerably better than the fits obtained in ALPO-11.[36] Our assignment of the shift tensor components is based on the discussion in the preceding paragraph. At the lowest loading, fitting yields $\delta_{\parallel}$ = 341 ppm. We are unaware of such large ^{129}Xe chemical shifts in a physisorbed state under ambient conditions. The shift is twice that observed in ALPO-11 or VA.[38] Notice that as the loading (and Xe−Xe interactions) increases, $\delta_{\parallel}$ decreases while $\delta_{\perp}$ increases slightly and δ_t remains constant. The loading dependence of the dynamically averaged shielding tensor is consistent with a slight increase in the tilt angle of the average Xe−Xe vector between adjacent occupied lattice sites. The loading dependence is dissimilar to that exhibited by ALPO-11, where both of the transverse shift tensor components increase with loading.[36] For the pressure range accessible in our SEOP apparatus, no inversion in the sign of the chemical shift anisotropy

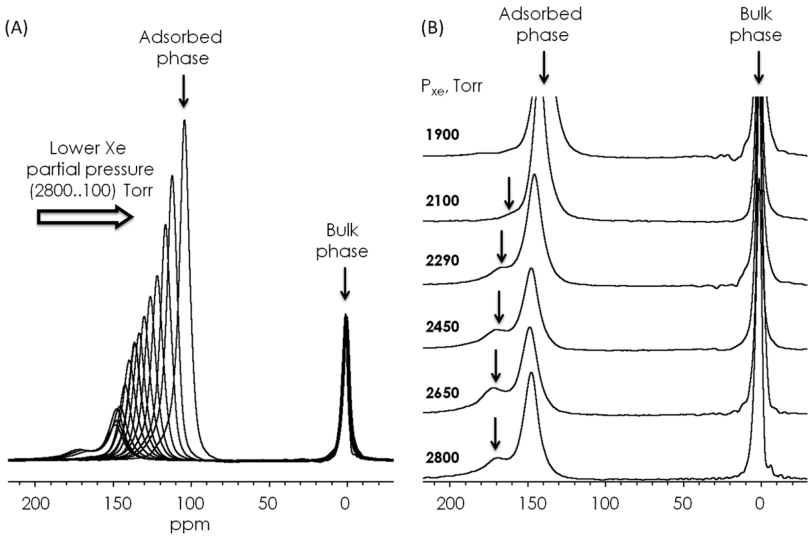

Figure 5. (A) Dependence of the ^{129}Xe line shape in the one-dimensional pores of the phenylethynylene bis-urea macrocycle 2 on Xe partial pressure from 100 to 2800 Torr. Experiments were performed using a HP Xe/He mixture at a total pressure of 3115 Torr at room temperature (25 °C). (B) The emergence of a secondary adsorption site at pressures above 1900 Torr is indicated by the arrows.

is observed. The Xe−Xe interactions are unable to exceed the strong lateral confinement of the bis-urea channel structure.

Upon increasing the pressure from 2650 to 2880 Torr, the isotropic shift varies continuously, but the powder pattern exhibits a discontinuous change and is insensitive to a further increase in Xe pressure. The invariance above 2880 suggests that at this pressure the loading is nearly complete. The short spin−lattice relaxation time T_{1c} observed in the HSTE data supports this assertion (see below).

The HP spectra for the larger macrocycle (**2**), where Xe is not so tightly confined as in **1**, are presented in Figure 5. The average chemical shift is substantially smaller and the line shape is symmetric, consistent with an effectively isotropic dynamically averaged electronic environment. Interestingly, a resolved smaller peak emerges at slightly higher chemical shift at pressures above 2100 Torr, which we tentatively assign to an ancillary pocket adsorption site. The trend in the shift of the main peak with pressure is shown in Figure 5B. The linear dependence indicates that the loading in **2** is far from saturation up to 2800 Torr.

Diffusion Dynamics. Due to the atomistic corrugation in nanochannels formed by the bis-urea macrocycles, diffusion of an isolated Xe atom is a thermally activated process involving hops between adjacent potential energy minima. The self-diffusion constant D_0 can be estimated from the Einstein−Smoluchowski equation

$$D_0 = \lambda^2/\tau \qquad (1)$$

where λ is the lattice parameter separating potential energy minima and τ is the hopping correlation time. With increasing time, Xe−Xe encounters begin to restrict the random-walk process, depending on the Xe density, and the details of the particle−particle interaction become relevant. For simple exclusion interaction in a single-file system, mutual exchange of positions in the lattice is prohibited, and the unrestricted RW process breaks down. The time-scaling of the mean-squared displacement (MSD) then enters the SFD regime, depending on the density.[56,65−75] The single-file criterion for spherically shaped molecules with collision diameter σ_c in smooth, rigid channels with cylindrical symmetry and internal diameter d is $d \geq \sigma_c \geq d/2$. Channels formed by macrocycle **1** fulfill the single-file criterion. For larger channels (*i.e.*, channels formed by stacking of macrocycle **2**) where $\sigma_c < d/2$, passages can occur and the MSD should scale as in normal unidimensional diffusion. The hallmark of SFD is the proportionality of the MSD to the square-root of the observation time[76,77]

$$\langle \Delta z^2 \rangle = 2F(\theta)t^{1/2} \qquad (2)$$

where

$$F(\theta) = \frac{1-\theta}{\theta}\lambda\sqrt{\frac{D_0}{\pi}} \qquad (3)$$

is known as the single-file mobility. For hypothetical infinitely long channels, the $\langle \Delta z^2 \rangle \propto t^{1/2}$ time-scaling persists indefinitely, but in finite-length channels, which are terminated by either blockages or openings to an external phase, a more complex behavior ensues. The MSD in single-file channels blocked at one or both ends will eventually plateau, entering a *restricted diffusion regime*.[32,42] In open-ended files, particle exchange with the bulk phase leads to a random walk of the center-of-mass (CM) of the particles in the file that is correlated to individual particle displacements.[56,66,67] CM diffusion is characterized by Fickian time-scaling, $\langle \Delta z^2 \rangle = 2D_{cm}t$,

with a reduced diffusivity D_{cm}. At sufficiently long time scales, CM ultimately dominates over SFD. Interestingly, molecular CM diffusion has never been reported in a molecule-nanochannel system, even though it is predicted to occur in the observation time-window of the PFG and HSTE NMR experiments.[31,32] Singly open ended channels do not support CM diffusion: diffusion in such channels enters a restricted regime. Therefore, one generally expects to observe a time-scaling $\langle \Delta z^2 \rangle^{1/2} \propto t^{a(t)}$, where $0 \leq a(t) \leq 1/2$, in a macroscopic ensemble of channels. In the single-file diffusion regime, $a = 1/4$. In larger channels, where mutual passes are not sterically hindered, as expected for Xe in the channels formed by **2**, $a(t) = 1/2$ is to be expected. In the restricted diffusion regime, $a(t) \rightarrow 0$ at sufficiently long t.

Molecular-exchange dynamics in open-ended channels can be accessed by the *tracer exchange* technique.[56,78] Tracer exchange monitors the uptake of labeled molecules by a porous material which is initially saturated with unlabeled molecules (or vice versa). The tracer exchange function is defined as

$$\gamma(t) \equiv \frac{n_{ads}(t)}{n_{ads}(\infty)} \tag{4}$$

where $n_{ads}(t)$ is the number of labeled molecules adsorbed after time t. The analogous expression for HSTE, which incorporates the spin−lattice relaxation of the tracer label, is given by the ratio of NMR signal of the adsorbed tracer species after a repolarization time t to its steady-state value:

$$\gamma_{NMR}(t) \equiv \frac{S_c(t)}{S_c(t \rightarrow \infty)} \tag{5}$$

The simple RW model for the HSTE function yields[25,32,42]

$$\gamma_{NMR}(t) = 1 - \frac{\Gamma(a, t/T_{1c})}{\Gamma(a)} \tag{6}$$

Equation 6 assumes constant a during the entire observation time window. For diffusion times $t \ll T_{1c}$, $S_c(t) \propto t^a$, and a remains as the single-fitting parameter in the model. The simple RW dynamics with simple interparticle exclusion interaction (*i.e.*, double occupancy of lattice sites is forbidden) can yield up to four distinct diffusion time regimes (not including ballistic transport at very short t).[42] This complexity is compounded by the effects of intermolecular interactions, adsorption barriers, and transport impedances, producing deviations from pure SFD or a shift of the crossover between different regimes. Noise in the data also contributes to error of fitted parameters. Equation 6 permits the assessment of the overall compliance to the idealized single-file diffusion model. The HSTE signals are collected and normalized to the steady state. An accurate steady-state signal is obtained by copious signal averaging in the fully recovered regime.

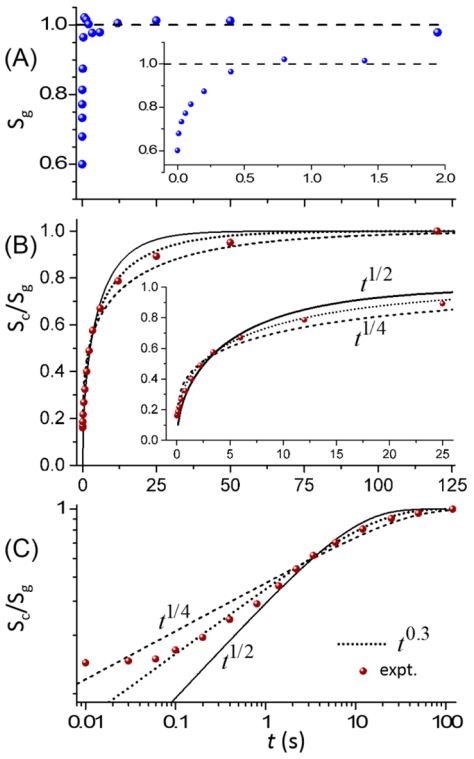

Figure 6. HP ^{129}Xe spin tracer exchange NMR in the phenyl ether bis-urea macrocycle 1 at −50 °C using 2600 Torr Xe at ∼150 mL/min. (A) Bulk gas-phase peak area normalized to the steady state. (B) Ratio of the channel-to-gas peak areas, normalized to the ratio in the steady state (red points). The dashed curve shows the best fit to eq 6 by fixing $a = 1/4$ (single-file diffusion) and allowing T_{1c} to vary; solid curve was obtained by fixing $a = 1/2$ and allowing T_{1c} to vary. Dotted curve is the best fit allowing both T_{1c} and a to vary. (C) Log representation of the same data and fits at short times. Raw spectra are provided in the Supporting Information.

HSTE utilizes a selective saturation-recovery pulse sequence in which the spin polarization of ^{129}Xe atoms initially located within the channels is destroyed by chemical-shift selective excitation, leaving the polarization of Xe atoms outside the sample unaffected. Recovery of the NMR signal of the adsorbed phase $S_c(t)$ back to the steady-state occurs by diffusion of unpolarized atoms to the file openings followed by exchange with hyperpolarized atoms exterior to the file.

Figures 6 and 7 present the results of the HSTE NMR experiments on our two bis-urea solids. Stacked plots of the processed spectra used to prepare these figures are presented in Figures S12 and S13 of the Supporting Information. The blue data points plotted in the top (A) panels represent the bulk gas phase HP ^{129}Xe peak areas normalized to the values obtained in the steady state. The ratios of the peak areas for the channel-adsorbed and bulk gas phase are normalized to the steady-state ratio, S_c/S_g, and plotted as dark red data points in the middle (B) panels, and the same data is shown on a log scale in the bottom (C) panels. Least-squares fitting to eq 6 was performed in three

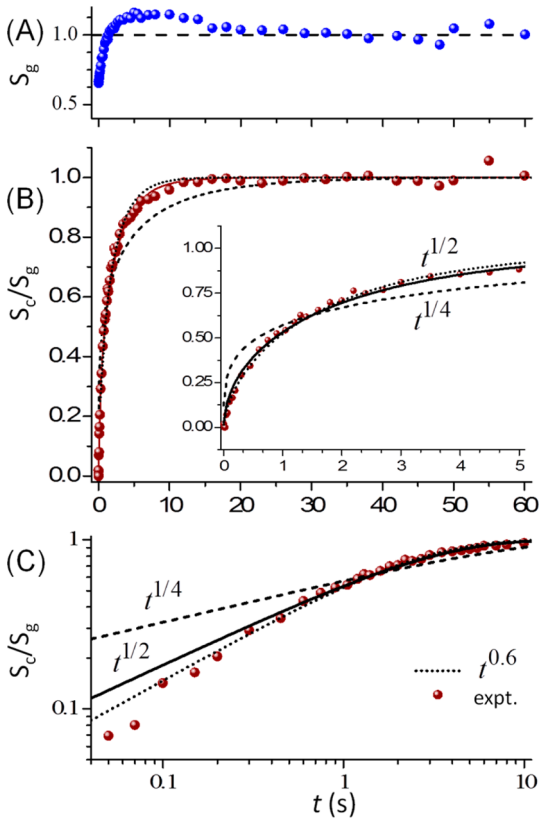

Figure 7. HP ^{129}Xe spin tracer exchange NMR in the phenylethynylene bis-urea macrocycle 2 at 25 °C using 2800 Torr Xe at ~70 mL/min flow rate. (A) Bulk gas-phase peak area normalized to the steady state. (B) Ratio of the channel-to-gas peak areas, normalized to the ratio in the steady state (red points). The dashed curve is the best fit to eq 6 fixing a = 1/4 (single-file diffusion) and allowing T_{1c} to vary. For the solid curve, a = 1/2 and T_{1c} is allowed to vary. Dotted line is the fit obtained allowing both T_{1c} and a to vary. (C) Log representation of same data. Raw spectra are provided in the Supporting Information.

ways: (i) fits to the model allowing both T_{1c} and a to vary as free parameters (dotted curves); (ii) fits obtained when T_{1c} is allowed to vary with the a parameter fixed to either 0.25 (for SFD) or 0.50 (ND), respectively (dashed and solid curves), and (iii) linear least-squares fitting to the linear region of $\log(S_c/S_g)$ *vs* $\log(t)$. Values for the fitted parameters are summarized in Table 1, and the fits obtained using methods (i) and (ii) are superimposed on the data in Figures 6 and 7. For macrocycle **1**, the values for the fitted parameters were reproduced (within the 90% confidence intervals) in two trials on the same synthetic batch. For macrocycle **2**, two different synthetic batches yielded consistent fitting results. The values of the a parameter obtained from linear least-squares fits to the log−log representation gave close agreement to the values reported in Table 1 for fitting method *ii*. The linear least-squares fits are included in Figures S14 of the Supporting Information.

In both Figure 6A and 7A, the gas-phase signal immediately following selective saturation of the adsorbed phase is seen to be depressed by ~40% relative

TABLE 1. Results of Nonlinear Least Squares Fitting of the Model, eq 6, to the HSTE Data Obtained in the Nanochannels of Macrocycles 1 and 2 Using All Three Fitting Methods (See Text)[a]

	fitting method	a	T_{1c} (s)	R^2
macrocycle **1**	*i*	0.25 (SFD)	50 ± 10	0.991
		0.50 (ND)	10 ± 2	0.981
	ii	0.30 ± 0.04	31 ± 11	0.993
	iii	0.32 ± 0.02	n/a	
macrocycle **2**	*i*	0.25 (SFD)	13 ± 2	0.983
		0.50 (ND)	3.8 ± 0.2	0.998
	ii	0.60 ± 0.04	2.9 ± 0.2	0.999
	iii	0.64 ± 0.04	n/a	

[a] Uncertainties represent 90% confidence intervals.

to the steady-state. A similar perturbation of the HP ^{129}Xe gas phase signal was reported in the HTSE study of the dipeptide VA.[31] Recovery occurs within about 0.75 s. Clearly, the assumption in our model that the bulk gas phase magnetization is unaffected by chemical exchange with the depolarized adsorbed phase is not rigorously obeyed for very short repolarization times. Therefore, the observed deviation in the HSTE data from the $t^{0.3}$ dependence (see Figure 6C) at repolarization times shorter than ~0.1 s is considered insignificant. For macrocycle **2**, the HSTE results presented in Figure 7 and Table 1 exhibit good compliance to the ND model, yielding consistent fitting results by all three methods and high R^2 obtained whether a is fixed to 0.5 or allowed to vary. When a is allowed to vary freely, it obtains a value of 0.60 ± 0.04, slightly higher than 0.5 as expected for ND. The data for t > 0.7 s show essentially perfect agreement to the ND model with a = 0.5.

The HSTE fitting results for the macrocycle **1** sample are reported in Figure 6 and Table 1. Clearly, the diffusion dynamics is dramatically altered by reducing the size of the center cavity. In contrast to the larger bis-urea macrocycle **2**, the HTSE data for macrocycle **1** exhibit better compliance to SFD (a = 0.25) than to ND (a = 0.5). A slight improvement in R^2 is obtained when a is allowed to vary, yielding a = 0.30 ± 0.04. This could be indicative of CM diffusion, as predicted by the analytical model for the observation times used in our HTSE experiment,[31] or it could be related to other factors not included in the simple analytical model, such as the distribution of channel persistence lengths, existence of singly open-ended channels, Xe clustering, momentum damping, or some combination of these effects. Notably, the data do not exhibit any significant time-dependence in a within the experimental observation window.

Previous ^{129}Xe NMR studies in other single-file nanochannels systems has shown that T_{1c} depends strongly on loading θ and channel diameter due to the dependence of the chemical shift relaxation mechanism on Xe−Xe collision dynamics.[25,26] The chemical shift and

observed spin relaxation time suggests the high loading regime ($\theta > 0.5$) for macrocycle **1** for the HSTE experiments at 2600 Torr Xe and −50 °C. The linearity of the pressure dependence of the chemical shift in **2** is consistent with the low-loading regime in the HSTE experiment at 2800 Torr, 25 °C.

CONCLUSIONS

Supramolecular self-assembly offers innumerable possibilities for synthesizing porous materials suitable for studies of spatial confinement effects on chemical reactions, gas adsorption/sequestration, controlled drug release, and molecular transport phenomena. The key advantage of this approach is that channel architecture is determined at the molecular building-block level.[79−84] Transition metal molecular wheels[26,82,84] provided an earlier example of a size-tunable supramolecular nanochannel system.[30] However, moisture/air sensitivity which can result in defects, blockages, and short persistence lengths make these materials less than optimal for fundamental transport studies. Paramagnetic impurities, which are detrimental to ^{129}Xe NMR measurements, are difficult to completely eliminate in the metal-based systems. The present work was motivated by the possibility to realize robust, hydrogen-bonded nanochannel materials with tunable structural properties. We employed HP ^{129}Xe NMR to probe intermoleular Xe interactions, channel architecture, and diffusion dynamics in the phenyl ether bis-urea and phenylethynylene macrocycles. The highly stable and robust crystals based on the bis-urea assembly motif are superior host materials for fundamental molecular transport studies.

Remarkably, we are able to report the NMR signal of strongly confined Xe atoms adsorbed into the channels formed by the phenyl ether bis-urea macrocycle **1**. Xenon can be accommodated only if its electron density undergoes a significant distortion from spherical symmetry, which results in a strong magnetic deshielding and anistropy. Shifts of up to 340 ppm are seen, surpassing even the chemical shift in solid Xe.[85,86] The ^{129}Xe chemical shift powder pattern reveals an asymmetric chemical shift tensor with three unique principal components. The pressure dependence of the line shape was analyzed in detail based on Jameson's theory. The powder pattern for macrocycle **1** shows a discontinuity at around 2600 Torr and becomes invariant to pressure thereafter, possibly due to reduced single-file mobility as the occupancy approaches unity or as a consequence of changes in packing or clustering in the channels. In contrast, the wider channels formed by phenylethynylene bis-urea macrocycle **2** yielded a much smaller deshielding and a symmetric line shape reflecting an isotropic dynamically averaged electronic environment. The adsorbed phase signal for bis-urea **2** macrocycles was found to scale linearly with Xe pressure up to 3115 Torr.

Our HSTE-NMR results conclusively demonstrate that bis-urea macrocycles are kinetically accessible to the gas phase. The diffusion of Xe through the channels formed by **1** is approximately single file in character, while the data in crystals of **2** are consistent with normal Fickian diffusion. Refinement of the diffusion model might be achieved by HTSE NMR experiments on single crystals (thereby eliminating effects of channel length distribution) or by measurements of bulk transport through bis-urea nanochannels in a membrane device.

As the porous solids studied here are assembled from molecular units (bis-urea macrocycles) that are readily synthesized from rigid spacers and protected ureas, the dimensions of the homogeneous channels can be controlled by the size of the macrocyclic units, allowing for precise and rational control over cavity dimensions, shape, channel architecture, and functionality. Notably, a predicted transition from Fickian diffusion to single-file diffusion dynamics was induced by a small molecular-level modification of the structure of the bis-urea spacer. To our knowledge, this is the first unequivocal demonstration of a structure-induced transitioning, achieved through rational design, from single-file to ordinary Fickian molecular diffusion dynamics on micrometer length scales. The high-fidelity, precisely uniform channels of the bis-ureas are thus established as hosts well-suited for molecular single-file diffusion studies.

MATERIALS AND METHODS

The syntheses of phenyl ether bis-urea (**1**) and phenylethynylene bis-urea (**2**) macrocycles were repeated as described in references 6 and 10−12. Needle-shaped crystals of the hosts were obtained by slow cooling either an AcOH solution of **1** (100 mg/50 mL from 120 °C at 1 °C/h) or a DMSO solution of **2** (150 mg/30 mL from 130 °C at 1 °C/h), respectively. The structures of the synthesized macrocycles were confirmed by single-crystal X-ray and high-resolution solution-state proton and carbon-13 NMR (see the Supporting Information, Figures S1−S3). Powder X-ray diffraction suggests that the bulk material is single phase (Supporting Information, Figures S7 and S8). Prior studies demonstrate that crystalline **1** and **2** are microporous and display type-I CO_2 adsorption isotherms with adsorption capacities of 316 and 349 m^2/g, respectively.[11,12] Host **1** is nonporous with both N_2 (g) and Ar (g), which have slightly larger kinetic diameters.[87] Although the Xe isotherms are unavailable, the accessible surface area in **1** is also expected to be small, considering its larger size relative to the other gases. Inspection of the SEM images of **1** prior to packing in the sample holder shows that the sample consists of rod-shaped crystallites with an average length of $250 \pm 90\ \mu m \times 3 \pm 2\ \mu m$ (Figure S9, Supporting Information).[11] SEM images of **2** reveal crystals with dimensions of $\sim 80 \pm 20\ \mu m \times 20 \pm 10\ \mu m$ (Figure S10, Supporting Information).[10,12]

The Rb−Xe SEOP polarizer is described in ref 52. Approximately 80 mg of solid was packed into a cylindrically shaped NMR sample holder machined from PEEK, threaded on both ends to accept PEEK compression fittings for $^1/_8$ in. OD PFA tubing.[40] The continuous stream of HP ^{129}Xe gas is transported

directly from the optical pumping cell outlet to the PEEK sample holder through the $^1/_8$ in. PFA tubing, which is routed through the probe body. Prior to the NMR measurements, the samples were evacuated to $\sim 10^{-3}$ Torr under dynamic vacuum at 110 °C for 6−8 h using a turbomolecular drag pump. Thermogravimetric analysis (see the Supporting Information, Figures S4−S6) was used to verify that this pretreatment was sufficient to fully remove solvent and leave the channels fully vacant for the adsorption of HP ^{129}Xe.

All NMR spectra presented in this work were acquired on a 9.4 T Bruker Avance 400 MHz wide-bore NMR spectrometer fitted with a Bruker wide-line solids probe, tuned and matched to 110.68859 MHz. HP ^{129}Xe NMR spectra in the crystals of **1** and **2** were acquired at 25 °C in continuous flow (CF) mode in which the Xe/He gas mixture is recirculated between the optical pumping cell and the sample holder.[25] Spectra were collected at a series of Xe partial pressures with a fixed total pressure of about 3000 Torr. The HP ^{129}Xe spectra were collected using a Hahn echo pulse sequence with 30 μs echo delay, a 3.25 μs $\pi/2$ pulse, and a 6.5 μs π pulse. For the sample containing macrocycle **1**, a minimum of 256 transients were signal averaged using a 4 s recycle delay. For **2,** 16 transients were averaged using a 1 s recycle delay. A 200 Hz Gaussian line broadening was applied to the free induction decay prior to Fourier Transformation. Least-squares fitting of the experimental line shapes for **1** to a single chemical shift powder pattern was carried out using DMFIT.[88] The reported best-fit values for the chemical shift tensor elements are referenced to the gas peak at low pressure.

The ^{129}Xe HSTE measurements were also performed in CF mode using mixtures of natural isotopic abundance Xe and helium.[25] A frequency-selective $\pi/2$ pulse train was applied to saturate the spin polarization of ^{129}Xe adsorbed inside the nanochannels. For macrocycle **1**, 32 transients were signal averaged at each repolarization delay ranging from 0.1 ms to 120 s. To increase the signal of the adsorbed phase, the temperature was lowered to −50 °C using the built-in variable temperature capability of the Bruker probe. For macrocycle **2**, which yielded much more intense adsorbed phase HP ^{129}Xe signals, eight transients were signal averaged for repolarization delays ranging from 0.1 ms to 60 s. The data was processed in MestraNova version 8.1.1 (MestraLab Research, S.L.). Free induction decays were apodized with a 200 Hz line broadening factor, Fourier transformed, and baseline corrected using cubic spline interpolation. Since the polarization of the gas may drift or fluctuate in time due to the various instrumental instabilities that affect the SEOP (*e.g.*, pumping cell temperature, Rb density, flow rate), the adsorbed phase signal was referenced to the gas by dividing peak integrals. The signal ratios were then normalized to the steady-state. For **1**, the HSTE experiments and fitting analysis were repeated twice on the same sample. For **2**, HSTE experiments and analysis were repeated in two different samples originating from different synthetic batches.

SEM Imaging. SEM micrographs of polycrystalline specimens of recrystallized **1** and **2** before packing into the NMR sample holder are shown in Figures S9 and S10 (Supporting Information).[11,12] SEM after packing were recorded using the FEG-SEM XL-40 microscope at the MAIC facility at the University of Florida. Comparison of the micrographs of **2** acquired before and after packing into the sample holder (Figure S11, Supporting Information) showed that averaged crystal length was affected somewhat by the packing/unpacking operation, but no attempt was made to quantify the change. Samples were recrystallized before reuse.

Conflict of Interest: The authors declare no competing financial interest.

Acknowledgment. Helpful discussions with S. Vasenkov (Department of Chemical Engineering, University of Florida) are gratefully acknowledged. This research was supported in part by the National Science Foundation (CHE-0957641 and CHE-1305136). Construction of the spin-exchange optical pumping setup was funded by the User Collaborative Grants Program at the National High Magnetic Field Laboratory, which is supported by National Science Foundation Cooperative Agreement No. DMR-1157490.

Supporting Information Available: The Supporting Information contains details of the synthesis, characterization, and SEM images of the materials used in this study. The Supporting Information is available free of charge on the ACS Publications website at DOI: 10.1021/acsnano.5b01895.

REFERENCES AND NOTES

1. Etter, M. C. Encoding and Decoding Hydrogen-Bond Patterns of Organic Compounds. *Acc. Chem. Res.* **1990**, *23*, 120–126.
2. Custelcean, R. Crystal Engineering with Urea and Thiourea Hydrogen-Bonding Groups. *Chem. Commun.* **2008**, 295–307.
3. Steed, J. W. Anion-Tuned Supramolecular Gels: A Natural Evolution from Urea Supramolecular Chemistry. *Chem. Soc. Rev.* **2010**, *39*, 3686–3699.
4. Volz, N.; Clayden, J. The Urea Renaissance. *Angew. Chem. Int. Edit* **2011**, *50*, 12148–12155.
5. Shimizu, L. S.; Salpage, S. R.; Korous, A. A. Functional Materials from Self-Assembled Bis-urea Macrocycles. *Acc. Chem. Res.* **2014**, *47*, 2116–2127.
6. Shimizu, L. S.; Hughes, A. D.; Smith, M. D.; Davis, M. J.; Zhang, B. P.; zur Loye, H. C.; Shimizu, K. D. Self-Assembled Nanotubes that Reversibly Bind Acetic Acid Guests. *J. Am. Chem. Soc.* **2003**, *125*, 14972–14973.
7. Yang, J.; Dewal, M. B.; Shimizu, L. S. Self-Assembling Bis-Urea Macrocycles Used as an Organic Zeolite for a Highly Stereoselective Photodimerization of 2-Cyclohexenone. *J. Am. Chem. Soc.* **2006**, *128*, 8122–8123.
8. Yang, J.; Dewal, M. B.; Sobransingh, D.; Smith, M. D.; Xu, Y. W.; Shimizu, L. S. Examination of the Structural Features That Favor the Columnar Self-Assembly of Bis-urea Macrocycles. *J. Org. Chem.* **2009**, *74*, 102–110.
9. Yang, J.; Dewal, M. B.; Profeta, S.; Smith, M. D.; Li, Y. Y.; Shimizu, L. S. Origins of Selectivity for the [2 + 2] Cycloaddition of Alpha,Beta-Unsaturated Ketones within a Porous Self-Assembled Organic Framework. *J. Am. Chem. Soc.* **2008**, *130*, 612–621.
10. Dawn, S.; Salpage, S. R.; Koscher, B. A.; Bick, A.; Wibowo, A. C.; Pellechia, P. J.; Shimizu, L. S. Applications of a Bis-Urea Phenylethynylene Self-Assembled Nanoreactor for [2 + 2] Photodimerizations. *J. Phys. Chem. A* **2014**, *118*, 10563–10574.
11. Dewal, M. B.; Lufaso, M. W.; Hughes, A. D.; Samuel, S. A.; Pellechia, P.; Shimizu, L. S. Absorption Properties of a Porous Organic Crystalline Apohost Formed by a Self-Assembled Bis-Urea Macrocycle. *Chem. Mater.* **2006**, *18*, 4855–4864.
12. Dawn, S.; Dewal, M. B.; Sobransingh, D.; Paderes, M. C.; Wibowo, A. C.; Smith, M. D.; Krause, J. A.; Pellechia, P. J.; Shimize, L. S. Self-Assembled Phenylethynylene Bis-urea Macrocycles Facilitate the Selective Photodimerization of Coumarin. *J. Am. Chem. Soc.* **2011**, *133*, 7025–7032.
13. Kärger, J. Straightforward Derivation of the Long-Time Limit of the Mean-Square Displacement in One-Dimensional Diffusion. *Phys. Rev. A* **1992**, *45*, 4173–4174.
14. Wei, Q. H.; Bechinger, C.; Leiderer, P. Single-File Diffusion of Colloids in One-Dimensional Channels. *Science* **2000**, *287*, 625–627.
15. Kollmann, M. Single-File Diffusion of Atomic and Colloidal Systems: Asymptotic Laws. *Phys. Rev. Lett.* **2003**, *90*, 180602.
16. Lutz, C.; Kollmann, M.; Bechinger, C. Single-File Diffusion of Colloids in One-Dimensional Channels. *Phys. Rev. Lett.* **2004**, *93*, 026001.
17. Chou, C. Y.; Eng, B. C.; Robert, M. One-Dimensional Diffusion of Colloids in Polymer Solutions. *J. Chem. Phys.* **2006**, *124*, 044902.
18. Herrera-Velarde, S.; Zamudio-Ojeda, A.; Castaneda-Priego, R. Ordering and Single-File Diffusion in Colloidal Systems. *J. Chem. Phys.* **2010**, *133*, 114902.
19. Mondal, C.; Sengupta, S. Single-File Diffusion and Kinetics of Template-Assisted Assembly of Colloids. *Phys. Rev. E* **2012**, *85*, 020402.
20. Yang, S. Y.; Yang, J. A.; Kim, E. S.; Jeon, G.; Oh, E. J.; Choi, K. Y.; Hahn, S. K.; Kim, J. K. Single-File Diffusion of Protein Drugs

through Cylindrical Nanochannels. *ACS Nano* **2010**, *4*, 3817–3822.
21. Gupta, V.; Nivarthi, S. S.; McCormick, A. V.; Davis, H. T. Evidence For Single File Diffusion of Ethane in the Molecular Sieve AlPO4-5. *Chem. Phys. Lett.* **1995**, *247*, 596–600.
22. Kukla, V.; Kornatowski, J.; Demuth, D.; Girnus, I.; Pfeifer, H.; Rees, L. V. C.; Schunk, S.; Unger, K. K.; Kärger, J. NMR Studies of Single-File Diffusion in Unidimensional Channel Zeolites. *Science* **1996**, *272*, 702–704.
23. Hahn, K.; Kärger, J.; Kukla, V. Single-File Diffusion Observation. *Phys. Rev. Lett.* **1996**, *76*, 2762–2765.
24. Meersmann, T.; Logan, J. W.; Simonutti, R.; Caldarelli, S.; Comotti, A.; Sozzani, P.; Kaiser, L. G.; Pines, A. Exploring Single-File Diffusion in One-Dimensional Nanochannels by Laser-Polarized Xe-129 NMR Spectroscopy. *J. Phys. Chem. A* **2000**, *104*, 11665–11670.
25. Cheng, C. Y.; Bowers, C. R. Observation of Single-File Diffusion in Dipeptide Nanotubes by Continuous-Flow Hyperpolarized Xenon-129 NMR Spectroscopy. *ChemPhysChem* **2007**, *8*, 2077–2081.
26. Cheng, C.-Y.; Stamatatos, T. C.; Christou, G.; Bowers, C. R. Molecular Wheels as Nanoporous Materials: Differing Modes of Gas Diffusion through Ga-10 and Ga-18 Wheels Probed by Hyperpolarized Xe-129 NMR Spectroscopy. *J. Am. Chem. Soc.* **2010**, *132*, 5387–5393.
27. Das, A.; Jayanthi, S.; Deepak, H. S. M. V.; Ramanathan, K. V.; Kumar, A.; Dasgupta, C.; Sood, A. K. Single-File Diffusion of Confined Water Inside SWNTs: An NMR Study. *ACS Nano* **2010**, *4*, 1687–1695.
28. Valiullin, R.; Kärger, J. Comment on "Single-File Diffusion of Confined Water Inside SWNTs: An NMR Study". *ACS Nano* **2010**, *4*, 3537–3537.
29. Das, A.; Ramanathan, K. V.; Kumar, A.; Dasgupta, C.; Sood, A. K. Reply to Comment by Valiullin and Kärger on Our Paper "Single-File Diffusion of Confined Water Inside SWNTs: An NMR Study". *ACS Nano* **2010**, *4*, 3537–3538.
30. Bowers, C. R.; Cheng, C.-Y.; Stamatatos, T. C.; Christou, G. Hyperpolarized NMR in Single-File Nanotubes. *AIP Conf. Proc.* **2011**, *1330*, 43–46.
31. Dvoyashkin, M.; Wang, A.; Vasenkov, S.; Bowers, C. R. Xenon in L-Alanyl-L-Valine Nanochannels: A Highly Ideal Molecular Single File System. *J. Phys. Chem. Lett.* **2013**, *4*, 3263–3267.
32. Dvoyashkin, M.; Bhase, H.; Mirnazari, N.; Vasenkov, S.; Bowers, C. R. Single-File Nanochannel Persistence Lengths from NMR. *Anal. Chem.* **2014**, *86*, 2200–2204.
33. Springuelhuet, M. A.; Fraissard, J. Xe-129 NMR of Xenon Adsorbed on the Molecular-Sieves AlPO4-11 and SAPO-11 - Chemical-Shift Anisotropy Related to the Asymmetry of the Adsorption Zones. *Chem. Phys. Lett.* **1989**, *154*, 299–302.
34. Chen, Q. J.; Springuelhuet, M. A.; Fraissard, J. Xe-129 NMR of Xenon Adsorbed on the Molecular-Sieves AlPO4-5, SAPO-5, MAPO-5, and SAPO-37. *Chem. Phys. Lett.* **1989**, *159*, 117–121.
35. Barrie, P. J.; Klinowski, J. Xe-129 NMR as a Probe for the Study of Microporous Solids - a Critical Review. *Prog. Nucl. Mag Res. Sp* **1992**, *24*, 91–108.
36. Ripmeester, J. A.; Ratcliffe, C. I. The Anisotropic Chemical-Shift of Xe-129 in the Molecular-Sieve AlPO-11 - a Dynamic Averaging Model. *J. Phys. Chem.* **1995**, *99*, 619–622.
37. Sozzani, P.; Comotti, A.; Simonutti, R.; Meersmann, T.; Logan, J. W.; Pines, A. A Porous Crystalline Molecular Solid Explored by Hyperpolarized Xenon. *Angew. Chem., Int. Ed.* **2000**, *39*, 2695–2698.
38. Moudrakovski, I.; Soldatov, D. V.; Ripmeester, J. A.; Sears, D. N.; Jameson, C. J. Xe NMR Lineshapes in Channels of Peptide Molecular Crystals. *Proc. Natl. Acad. Sci. USA* **2004**, *101*, 17924–17929.
39. Soldatov, D. V.; Moudrakovski, I. L.; Grachev, E. V.; Ripmeester, J. A. Micropores in Crystalline Dipeptides as Seen from the Crystal Structure, He Pycnometry, and Xe-129 NMR Spectroscopy. *J. Am. Chem. Soc.* **2006**, *128*, 6737–6744.
40. Cheng, C. Y.; Bowers, C. R. Direct Observation of Atoms Entering and Exiting L-Alanyl-L-Valine Nanotubes by Hyperpolarized Xenon-129 NMR. *J. Am. Chem. Soc.* **2007**, *129*, 13997–14002.
41. Anedda, R.; Soldatov, D. V.; Moudrakovski, I. L.; Casu, M.; Ripmeester, J. A. A New Approach to Characterizing Sorption in Materials with Flexible Micropores. *Chem. Mater.* **2008**, *20*, 2908–2920.
42. Bowers, C. R., Characterization of Single-File Diffusion in Nanotubes. In *Hyperpolarized Xenon-129 Magnetic Resonance*; Meersmann, T., Brunner, E., Eds.; The Royal Society of Chemistry Publishing: Cambridge, 2015.
43. Jameson, C. J.; Jameson, A. K.; Cohen, S. M. Temperature and Density Dependence of Xe-129 Chemical-Shift in Xenon Gas. *J. Chem. Phys.* **1973**, *59*, 4540–4546.
44. Jameson, C. J.; de Dios, A. C. Xe Nuclear Magnetic Resonance Line Shapes in Nanochannels. *J. Chem. Phys.* **2002**, *116*, 3805–3821.
45. Moudrakovski, I. L.; Nossov, A.; Lang, S.; Breeze, S. R.; Ratcliffe, C. I.; Simard, B.; Santyr, G.; Ripmeester, J. A. Continuous Flow NMR with Hyperpolarized Xenon for the Characterization of Materials and Processes. *Chem. Mater.* **2000**, *12*, 1181–1183.
46. Cates, G. D.; Benton, D. R.; Gatzke, M.; Happer, W.; Hasson, K. C.; Newbury, N. R. Laser Production of Large Nuclear-Spin Polarization in Frozen Xenon. *Phys. Rev. Lett.* **1990**, *65*, 2591–2594.
47. Raftery, D.; Long, H.; Meersmann, T.; Grandinetti, P. J.; Reven, L.; Pines, A. High-Field NMR of Adsorbed Xenon Polarized by Laser Pumping. *Phys. Rev. Lett.* **1991**, *66*, 584–587.
48. Driehuys, B.; Cates, G. D.; Miron, E.; Sauer, K.; Walter, D. K.; Happer, W. High-Volume Production of Laser-Polarized Xe-129. *Appl. Phys. Lett.* **1996**, *69*, 1668–1670.
49. Haake, M.; Pines, A.; Reimer, J. A.; Seydoux, R. Surface-Enhanced NMR Using Continuous-Flow Laser-Polarized Xenon. *J. Am. Chem. Soc.* **1997**, *119*, 11711–11712.
50. Brunner, E.; Haake, M.; Kaiser, L.; Pines, A.; Reimer, J. A. Gas Flow MRI Using Circulating Laser-Polarized Xe-129. *J. Magn. Reson.* **1999**, *138*, 155–159.
51. Song, Y. Q.; Goodson, B. M.; Pines, A. NMR and MRI Using Laser-Polarized Xenon. *Spectroscopy* **1999**, *14*, 26–33.
52. Zook, A. L.; Adhyaru, B. B.; Bowers, C. R. High Capacity Production of > 65% Spin Polarized Xenon-129 for NMR Spectroscopy and Imaging. *J. Magn. Reson.* **2002**, *159*, 175–182.
53. Simonutti, R.; Bracco, S.; Comotti, A.; Mauri, M.; Sozzani, P. Continuous Flow Hyperpolarized Xe-129 NMR for Studying Porous Polymers and Blends. *Chem. Mater.* **2006**, *18*, 4651–4657.
54. Rodenbeck, C.; Kärger, J.; Hahn, K. Tracer Exchange and Catalytic Reaction in Single-File Systems. *J. Catal.* **1995**, *157*, 656–664.
55. Rodenbeck, C.; Kärger, J.; Hahn, K. Exact Analytical Description of Tracer Exchange and Particle Conversion in Single-File Systems. *Phys. Rev. E* **1997**, *55*, 5697–5712.
56. Vasenkov, S.; Kärger, J. Different Time Regimes of Tracer Exchange in Single-File Systems. *Phys. Rev. E* **2002**, *66*, 052601.
57. Kärger, J. Measurement of Diffusion in Zeolites - A Never Ending Challenge? *Adsorption* **2003**, *9*, 29–35.
58. Brauer, P.; Brzank, A.; Kärger, J. Adsorption and Reaction in Single-File Networks. *J. Phys. Chem. B* **2003**, *107*, 1821–1831.
59. Gulin-Gonzalez, J.; Schuring, A.; Fritzsche, S.; Kärger, J.; Vasenkov, S. The Influence of the Desorption Barrier on the Transport of Molecules Through the External Surface of Nanoporous Crystals. *Chem. Phys. Lett.* **2006**, *430*, 60–66.
60. Heinke, L.; Tzoulaki, D.; Chmelik, C.; Hibbe, F.; van Baten, J. M.; Lim, H.; Li, J.; Krishna, R.; Kärger, J. Assessing Guest Diffusivities in Porous Hosts from Transient Concentration Profiles. *Phys. Rev. Lett.* **2009**, *102*, 065901.
61. Iliyas, A.; Eic, M.; Zahedi-Niaki, M. H.; Vasenkov, S. Toward Observation of Single-File Diffusion Using the Tracer Zero-Length Column Method. *J. Phys. Chem. B* **2008**, *112*, 3821–3825.

62. Shimizu, L. S.; Hughes, A. D.; Smith, M. D.; Samuel, S. A.; Ciurtin-Smith, D. Assembled Columnar Structures from Bis-Urea Macrocycles. *Supramol Chem.* **2005**, *17*, 27–30.
63. *CCDC Mercury - Crystal Structure Visualisation, Exploration, and Analysis Software*; University of Cambridge: Cambridge, 2015.
64. Macrae, C. F.; Edgington, P. R.; McCabe, P.; Pidcock, E.; Shields, G. P.; Taylor, R.; Towler, M.; van De Streek, J. Mercury: Visualization and Analysis of Crystal Structures. *J. Appl. Crystallogr.* **2006**, *39*, 453–457.
65. Sholl, D. S.; Fichthorn, K. A. Normal, Single-File, and Dual-Mode Diffusion of Binary Adsorbate Mixtures in AlPO4-5. *J. Chem. Phys.* **1997**, *107*, 4384–4389.
66. Hahn, K.; Kärger, J. Deviations from the Normal Time Regime of Single-File Diffusion. *J. Phys. Chem. Lett.* **1998**, *102*, 5766–5771.
67. Nelson, P. H.; Auerbach, S. M. Self-Diffusion in Single-File Zeolite Membranes is Fickian at Long Times. *J. Chem. Phys.* **1999**, *110*, 9235–9243.
68. Brzank, A.; Schutz, G. M.; Brauer, P.; Kärger, J. Molecular Traffic Control in Single-File Networks with Fast Catalysts. *Phys. Rev. E: Stat., Nonlinear, Soft Matter Phys.* **2004**, *69*, 031102/1–031102/5.
69. Schuring, A.; Vasenkov, S.; Fritzsche, S. Influence of Boundaries of Nanoporous Crystals on Molecular Exchange under the Conditions of Single-File Diffusion. *J. Phys. Chem. B* **2005**, *109*, 16711–16717.
70. Vasenkov, S.; Schuring, A.; Fritzsche, S. Single-File Diffusion Near Channel Boundaries. *Langmuir* **2006**, *22*, 5728–5733.
71. Schuering, A.; Fritzsche, S.; Vasenkov, S. A New Type of Diffusional Boundary Effect at the Edges of Single-File Channels. *Stud. Surf. Sci. Catal.* **2007**, *170A*, 1000–1007.
72. Bandyopadhyay, T. Single-File Diffusion Through Inhomogeneous Nanopores. *J. Chem. Phys.* **2008**, *128*, 114712.
73. Burada, P. S.; Hanggi, P.; Marchesoni, F.; Schmid, G.; Talkner, P. Diffusion in Confined Geometries. *ChemPhysChem* **2009**, *10*, 45–54.
74. Bauer, M.; Valiullin, R.; Radons, G.; Kärger, J. How to Compare Diffusion Processes Assessed by Single-Particle Tracking and Pulsed Field Gradient Nuclear Magnetic Resonance. *J. Chem. Phys.* **2011**, *135*, 144118.
75. Delfau, J. B.; Coste, C.; Saint Jean, M. Single-File Diffusion of Particles with Long-Range Interactions: Damping and Finite-Size Effects. *Phys. Rev. E* **2011**, *84*, 011101.
76. Levitt, D. G. Dynamics of a Single-File Pore: Non-Fickian Behavior. *Phys. Rev. A* **1973**, *8*, 3050.
77. Kärger, J. Long-Time Limit of the Self-Correlation-Function of One-Dimensional Diffusion. *Phys. Rev. E* **1993**, *47*, 1427–1428.
78. Schuring, A.; Vasenkov, S.; Fritzsche, S. Influence of Boundaries of Nanoporous Crystals on Molecular Exchange Under the Conditions of Single-File Diffusion. *J. Phys. Chem. B* **2005**, *109*, 16711–16717.
79. Bein, T. Supramolecular Architecture. In *Supramolecular Architecture*; American Chemical Society: Washington, DC, 1992; pp 1−7.
80. Lehn, J. M. Toward Complex Matter: Supramolecular Chemistry and Self-Organization. *Proc. Natl. Acad. Sci. U.S.A.* **2002**, *99*, 4763–4768.
81. Hof, F.; Craig, S. L.; Nuckolls, C.; Rebek, J. Molecular Encapsulation. *Angew. Chem. Int. Edit* **2002**, *41*, 1488–1508.
82. Tasiopoulos, A. J.; Vinslava, A.; Wernsdorfer, W.; Abboud, K. A.; Christou, G. Giant Single-Molecule Magnets: A Mn84 Torus and Its Supramolecular Nanotubes. *Angew. Chem., Int. Ed.* **2004**, *43*, 2117–2121.
83. Soldatov Dmitriy, V., Stimuli-Responsive Supramolecular Solids: Functional Porous and Inclusion Materials. In *Stimuli-Responsive Polymeric Films and Coatings*; American Chemical Society: Washington, DC, 2005; pp 214−231.
84. King, P.; Stamatatos, T. C.; Abboud, K. A.; Christou, G. Reversible Size Modification of Iron and Gallium Molecular Wheels: A Ga-10 "Gallic Wheel" and Large Ga-18 and Fe-18 Wheels. *Angew. Chem., Int. Ed.* **2006**, *45*, 7379–7383.
85. Long, H. W.; Gaede, H. C.; Shore, J.; Reven, L.; Bowers, C. R.; Kritzenberger, J.; Pietrass, T.; Pines, A.; Tang, P.; Reimer, J. A. High-Field Cross-Polarization NMR From Laser-Polarized Xenon to a Polymer Surface. *J. Am. Chem. Soc.* **1993**, *115*, 8491–8492.
86. Brinkmann, D. Nuclear Magnetic Resonance Shift of Xe129 in Solid Xenon. *Phys. Rev. Lett.* **1964**, *13*, 187–188.
87. Dewal, M. B. *Design, Synthesis, and Applications of Porous Crystals From Self-Assembled Bis-Urea Macrocycles*; University of South Carolina: Columbia, 2008.
88. Massiot, D.; Fayon, F.; Capron, M.; King, I.; Le Calve, S.; Alonso, B.; Durand, J. O.; Bujoli, B.; Gan, Z. H.; Hoatson, G. Modelling One- and Two-Dimensional Solid-State NMR Spectra. *Magn. Reson. Chem.* **2002**, *40*, 70–76.